2019

Effect of Temperature and Strain Rate on the Hot Deformation Behaviour of Ferritic Stainless Steel

Guoqing Zu
University of Wollongong, Changchun University of Technology, gz854@uowmail.edu.au

Yukuan Lu
Changchun University of Technology

Yi Yan
Nanchang Hangkong University, University of Wollongong, yy619@uowmail.edu.au

Xiaoming Zhang
Northeastern University, zhang_xiaoming@163.com

Jingwei Zhao
University of Wollongong, jzhao@uow.edu.au

See next page for additional authors

Effect of Temperature and Strain Rate on the Hot Deformation Behaviour of Ferritic Stainless Steel

Abstract

The flow behaviour and microstructure characteristics of a ferritic stainless steel were investigated using plain strain compression test on a Gleeble 3500 thermo-mechanical test simulator with a hydrawedge system in the temperature range of 850-1100 °C and strain rate range of 0.1-50 s^{-1}. The phenomenological constitutive model and the relationship between the Zener-Hollomon (Z) parameter and flow stress were established. The results reveal that the flow softening phenomenon occurs at high strain rate, which is caused by the coupling effect of the adiabatic heating and dynamic recrystallisation (DRX). New grains nucleate preferentially at the original grain boundaries by strain-induced grain boundary migration. With an increase of temperature or strain rate, a part of new grains form in the interior of deformed grains. The DRX grain size and fraction increase with the increase of temperature, however, exhibit a non-linear relationship with strain rate.

Disciplines

Engineering | Science and Technology Studies

Publication Details

Zu, G., Lu, Y., Yan, Y., Zhang, X., Zhao, J., Du, W., Ran, X. & Jiang, Z. (2019). Effect of Temperature and Strain Rate on the Hot Deformation Behaviour of Ferritic Stainless Steel. Metals and Materials International, Online First 1-12.

Authors

Guoqing Zu, Yukuan Lu, Yi Yan, Xiaoming Zhang, Jingwei Zhao, Wei Du, Xu Ran, and Zhengyi Jiang

Effect of temperature and strain rate on the hot deformation behaviour of ferritic stainless steel

Guoqing Zu[a, b], Yukuan Lu[a], Yi Yan[b, c], Xiaoming Zhang[d], Jingwei Zhao[b, *], Wei Du[e], Xu Ran[a], Zhengyi Jiang[b,*]

a Key Laboratory of Advanced Structural Materials of Ministry of Education, Changchun University of Technology, Changchun 130012, PR China

b School of Mechanical, Materials and Mechatronic Engineering, University of Wollongong, NSW 2522, Australia

c School of Materials Science and Engineering, Nanchang Hangkong University, Nanchang 330063, China

d State Key Laboratory of Rolling and Automation, Northeastern University, Shenyang 110819, PR China

e Stainless Steel Technical Centre, Baosteel Research Institute (R&D Centre), Baoshan Iron & Steel Co., Ltd., Shanghai 200431, China

Abstract

The flow behaviour and microstructure characteristics of ferritic stainless steel were investigated using plain strain compression test with a true strain of 90% in the temperature range of 850-1100 °C and strain rate of 0.1-50 s^{-1} on a Gleeble 3500 thermal-mechanical test simulator with a hydrawedge system. The phenomenological constitutive model and the relationship between the Zener-Hollomon parameter and flow stress were established. The results reveal that the flow softening phenomenon occurred at the high strain rate, which was caused by the coupling effect of the adiabatic heating and dynamic recrystallization. The new grains nucleated preferentially at original grain boundaries by strain-induced grain boundary migration. With an increase of deformation temperature or strain rate, a part of new grains formed in the interior of deformed grains. The dynamic recrystallization grain size and fraction increase with the increase of the deformation temperature, however, exhibite a non-linear relationship with strain rate.

*Corresponding authors.

E-mail addresses: gz854@uowmail.edu.au (G. Zu), jzhao@uow.edu.au (J. Zhao), jiang@uow.edu.au (Z. Jiang)

1. Introduction

Ferritic stainless steel (FSS), typically, containing about 13 wt.% to 30 wt.% chromium to increase corrosion resistance, is extensively used in exhaust pipes, kitchen wares, home appliances, food industry [1-4]. FSS offers various advantages in comparison with austenitic stainless steel, such as the excellent stress corrosion cracking resistance, high thermal conductivity and good corrosion resistance [5, 6]. Even more important, no or very low nickel content, FSS is a more cost-effective alternative to expensive austenitic stainless steel, and indeed erode the market share of the latter gradually [7, 8]. However, traditional FSS exhibits poor low-temperature toughness, high notch sensitivity, and susceptible intergranular corrosion. It is generally realised that the shortcomings, mainly connect with the content of C and N [2, 8-11]. 430LR is a new type of FSS developed by Baosteel, reducing C and N contents and adding Nb, Ti and Sn elements in comparison to conventional 430 FSS.

430LR FSS developed by Baosteel is ferritic at all temperatures, therefore, no austenite-to-ferrite phase transformation appears during hot deformation. Ferritic steel with high stacking fault energy, it is generally accepted that the dominated softening mechanism is dynamic recovery (DRV) [12-14]. However, some researchers have reported that the dynamic recrystallization (DRX) can be obtained in some case [3, 15-20]. The dynamic restoration behaviour intensely depends on the deformation conditions [3, 15, 21-25]. Thermo-mechanical processing is a significant step to manufacture FSS, not only for reducing thickness, but also receiving desirable microstructure and texture. If after hot processing, the initial as-cast columnar grains turn into serious elongated bands, which is difficult to eliminate in subsequent working. It is one of the most important reasons to cause ridging in tensile text or deep drawing [1, 2, 8, 26]. The hot deformation process is considered complex, involving flow instability, work hardening, DRV, and DRX. An in-depth understanding of the relationship between the deformation behaviour and the processing parameters, such as the deformation temperature and strain rate, is significant for controlling the microstructure and improving the mechanical properties [27, 28].

The constitutive modelling and microstructure characteristics are the two major technologies applied to describe the deformation mechanism and optimize deformation parameters. An accurate constitutive model is essential for calculating hot rolling force and computer simulation the forming processes of the alloy [29-31]. The understanding of microstructure characteristics under different hot deformation parameters is quite significant to optimize the workability and achieving microstructural control from an engineering viewpoint [16]. Mehtonen et al. [3] established a constitutive equation which well describes the flow stress as a function of strain, strain rate, and temperature. They also pointed out the relationship between Zener-Homon parameter and dynamic restoration mechanism [18]. In addition, by studying the hot deformation behaviour of FSS with different chromium content, they found that the flow stress was a function of the Cr content because of solid solution strengthening the effect of Cr [32]. However, in their research works, the strain rate range of 0.01-1 s^{-1} and deformation temperature range of 950-1050 °C were limited to supply the referential meaning to industrial manufacture. By studying the hot deformation of an ultra-pure 17% Cr FSS, Gao et al. [9] showed the microstructural evolution and the modified constitutive equation, while the maximum true strain less than 60%. The substructure and dynamic softening in low strain

rates during hot deformation of a 26% Cr FSS were studied by Gao et al. [14], but not involved the deformation behaviour in high strain rate. Therefore, a systematic investigation is still needed in FSS under isothermal deformation with a wider range of processing conditions and a larger true strain [16].

In this study, plastic deformation behaviour of 430LR FSS was investigated using plane strain compression tests under a high strain and wide ranges of deformation temperatures and strain rates, which overlap the conditions in the manufacturing of FSS. The effects of deformation temperature and strain rate on the flow behaviour on the FSS were described. The constitutive equations of the FSS were established to investigate the hot deformation mechanism, provide a reference for the optimization of hot working. Also, the dynamic restoration characteristics in 430LR FSS under various conditions were systematically investigated.

2. Experimental procedure

The chemical composition of the 430LR FSS is listed in Table 1. The microstructure of the steel before plane strain compression tests is shown in Fig. 1, from which the typical ferritic microstructure with an average grain size of 82 μm can be clearly observed. Tests specimens have the dimension of 20 mm×15 mm×8 mm.

Table 1 Chemical compositions of the 430LR FSS (in wt.%)

	C	Si	Mn	S	P	Cr	N	Nb	Ti	Sn
430LR	0.0101	0.31	0.19	0.002	0.024	16.58	0.012	0.15	0.11	0.009

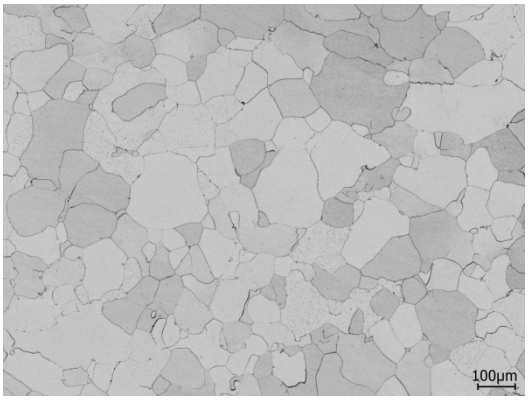

Fig. 1. The initial microstructure of the 430LR stainless steel

The hot plane strain compression tests were performed using a Gleeble 3500 thermal-mechanical test simulator with a hydrawedge system which offers excellent physical simulation capabilities for optimizing hot rolling [33]. A single pass large strain compression was imposed without holding, reheating or secondary deformation between the processing steps. Therefore, eliminated multivariate influences on the deformation behaviours. The schematic of the plant strain compression and the process route is shown in Fig. 2. In order to reduce the friction during compression and to avoid bonding of the specimens to the anvil surfaces, graphite foils and tantalum sheet were used between the surface of anvils and specimens in the deformation area. Prior to plant strain compression, the specimens were resistance reheated to 1120 °C at a rate of 20 °C/s, held for

60 s to homogenize the microstructure, and then cooled to the compression temperature(850, 900, 950, 1000, 1050 and 1100 °C) with a cooling rate of 10 °C/s. The specimens were also held at the compression temperature for 60 s to eliminate the thermal gradient before deformation tests. The specimens were compressed up to a true strain of 0.9 in a single pass hit with the strain rates of 0.1, 1, 10 and 50 s^{-1}. After compression, the specimens were immediately quenched in situ by a water jet for preserving the isothermal deformed microstructures. The compressed specimens were cut along the longitudinal section composed by rolling direction (RD) and normal direction (ND) for microstructural observations, as shown in Fig. 2(a).

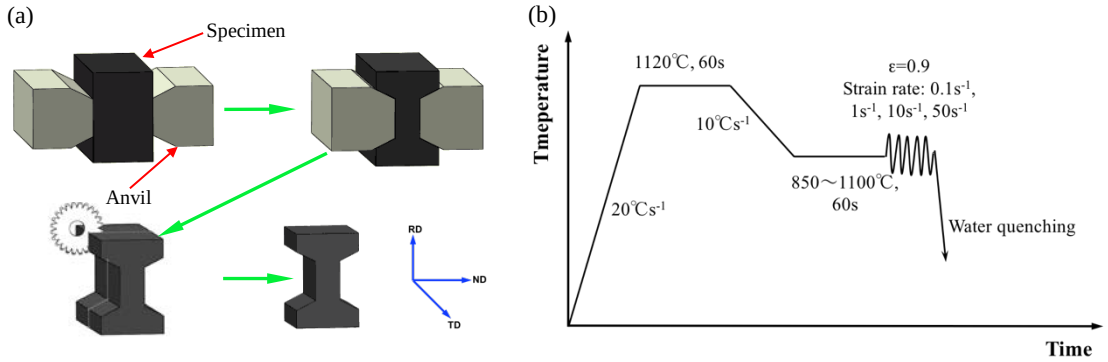

Fig. 2. Schematic illustration of (a) the plant stress compression, and (b) the hot deformation schedule

3. Results and discussion

3.1 Flow stress behaviour

The flow stress curves during plane strain compression tests are presented in Fig. 3. It can be observed that the flow stress is sensitively dependent on the strain rate and deformation temperature. The flow stress increases significantly with the increase of the strain rate at a given strain rate and decreases with the increase of the temperature at the same strain rate. At low strain rate (0.1 and 1 s^{-1}), the flow stress curves exhibit a short hardening stage followed by a slight working hardening under 850, 900 and 950 °C, except at 850 °C in 0.1 s^{-1}. When the temperature increased to 1000 °C or higher, the flow stress curves show steady-state stress or slight softening stage after the strain of 0.2. Such behaviour is the results of the interaction between the dislocation multiplication and the dynamic restoration. At lower temperature, the total dislocation density continuously increases, causing the work hardening. In contrast, at the higher temperature, the dislocation annihilation and recombination by DRV, as well as DRX, can balance or overcome the dislocation multiplication by the compression.

Mehtonen et al. [3] reported at high temperature and low strain rate there is hardly continuous work hardening, while the flow stress increasing steadily at the higher strain rate. In the present study, at the higher strain rate of 10 and 50 s^{-1}, all the flow stress flow stress curves, however, show slowly continuous flow softening after peak stress. Zhao et al. [31] observed a similar phenomenon in cylindrical isothermal compression of 430 FSS, but no intensive study. Han et al. [34] pointed out that the hot deformation is not an isothermal process. At the strain rate of 10 s^{-1}, the temperature can rise by 17.8 °C with strain increasing, which result in the flow stress decreasing during compression.

By formula calculating, Liu et al. [35] indicated that the temperature increase 3 to 31 °C leading to a flow softening from 2.5 to 42.4 MPa in the strain rate of 0.001 to 10 s^{-1}. In the present study, the system recorded the test date at a frequency of 2000 point per second, therefore, all the detail changes of temperature can be detected during the whole compression process. According to the whole time-temperature curves collected by the temperature sensor, obvious evidence demonstrated that there is temperature fluctuation during compression, especially for low temperature and high strain rate. At 850 and 1100 °C with the strain rate of 50 s^{-1}, the deformation temperature increase 39 and 19 °C in an instant, respectively, as an insert in Fig. 3(a, f). It can be concluded that the adiabatic temperature rise is one of the most significant factors on the softening phenomenon of 430LR FSS at high strain rate conditions. The effect of microstructural changing on flow behaviour will be analysed in the following section.

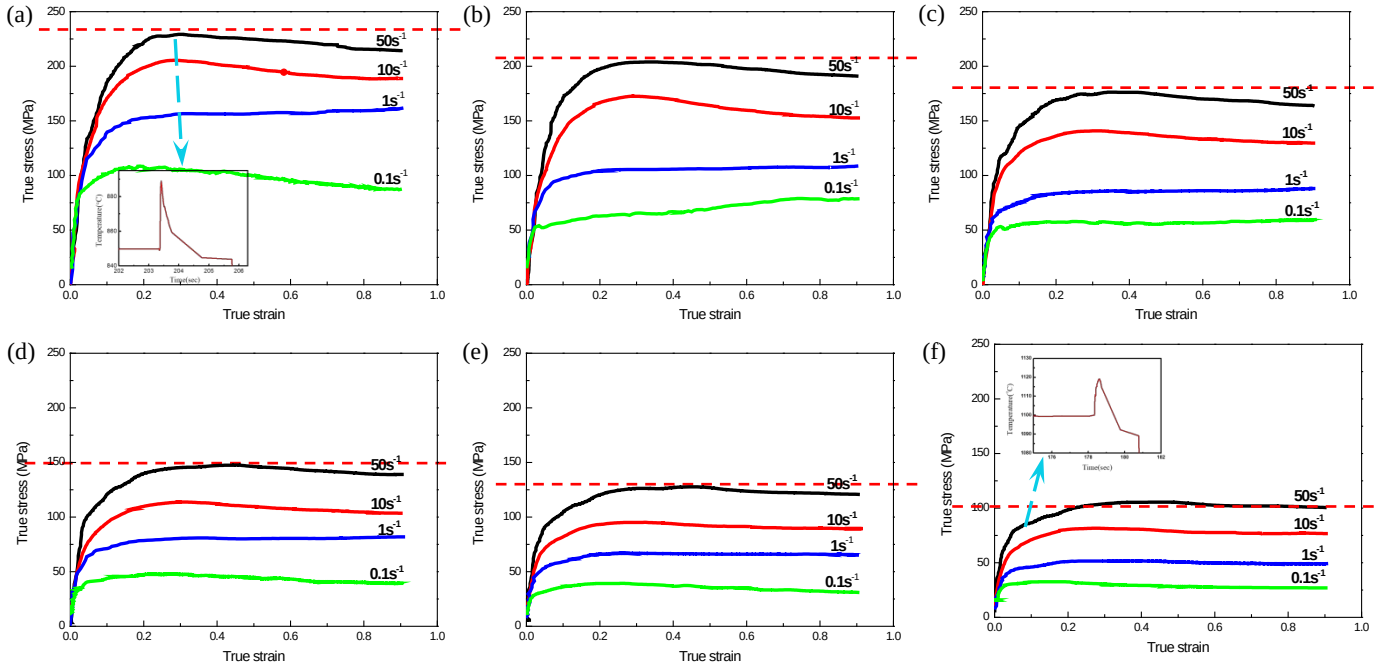

Fig. 3 Flow stress curves of the 430lr FSS deformed at strain rates of 0.1-50s^{-1} at (a) 850 °C, (b) 900 °C, (c) 950 °C, (d) 1000 °C, (e) 1050 °C, and (f) 1100 °C

3.2 Constitutive equations

Several constitutive models have been proposed to characterise the hot deformation behaviour. Arrhenius-type phenomenological constitutive model is the most widely used to investigate the effects of strain rate, temperature, and strain on the flow stress behaviour of metals at elevated temperatures [36]. Three types of Arrhenius-type equations, which proposed by Sellars and McTegart, are expressed as follows [37]:

$$\dot{\varepsilon} = A_1 \sigma^{n_1} \exp(-\frac{Q}{RT}) \quad \text{(Power function)} \tag{1}$$

$$\dot{\varepsilon} = A_2 \exp(n_2 \sigma) \exp(-\frac{Q}{RT}) \quad \text{(exponential function)} \tag{2}$$

$$\dot{\varepsilon} = A[\sinh(\alpha\sigma)]^n \exp(-\frac{Q}{RT}) \quad \text{(hyperbolic function)} \tag{3}$$

where $\dot{\varepsilon}$ is the strain rate, A_1, A_2 and A are material constant, σ is the flow stress, n_1, n_2, and n are the stress exponent, Q is the activation energy of hot deformation, R is the gas constant, and T is the absolute temperature. α is the stress multiplier, and can be expressed as:

$$\alpha \approx \frac{n_2}{n_1} \tag{4}$$

The power function and the exponential function are used at the lower and higher stress level, respectively. The hyperbolic function, however, can be applied for all the stress level. Moreover, the combined effect of temperature and strain rate on the hot deformation behaviour can be represented by the Zener-Hollomon (Z) parameter in an exponent type equation as [38]:

$$Z = \dot{\varepsilon} \exp(\frac{Q}{RT}) \tag{5}$$

Taking natural logarithm of both sides of Eqs. (1)-(3), respectively, the new equations can be expressed as:

$$\ln \dot{\varepsilon} = \ln A_1 + n_1 \ln \sigma - (\frac{Q}{RT}) \quad \text{(Power function)} \tag{6}$$

$$\ln \dot{\varepsilon} = \ln A_2 + n_2 \sigma - (\frac{Q}{RT}) \quad \text{(exponential function)} \tag{7}$$

$$\ln \dot{\varepsilon} = \ln A + n \ln[\sinh(\alpha\sigma)] - (\frac{Q}{RT}) \quad \text{(hyperbolic function)} \tag{8}$$

From Eqs. (6) and (7), the parameters n_1 and n_2 can be obtained respectively from the slopes of the $\ln \dot{\varepsilon}$ against $\ln \sigma$ and the $\ln \dot{\varepsilon}$ against σ plots, as shown in Fig. 4. According to Eq. (4), the value of α can be calculated. Substituting the value of α into Eq. (8), then, the parameter n can be acquired by the slopes of $\ln \dot{\varepsilon}$ against $\ln[\sinh(\alpha\sigma)]$, as shown in Fig. 5(a).

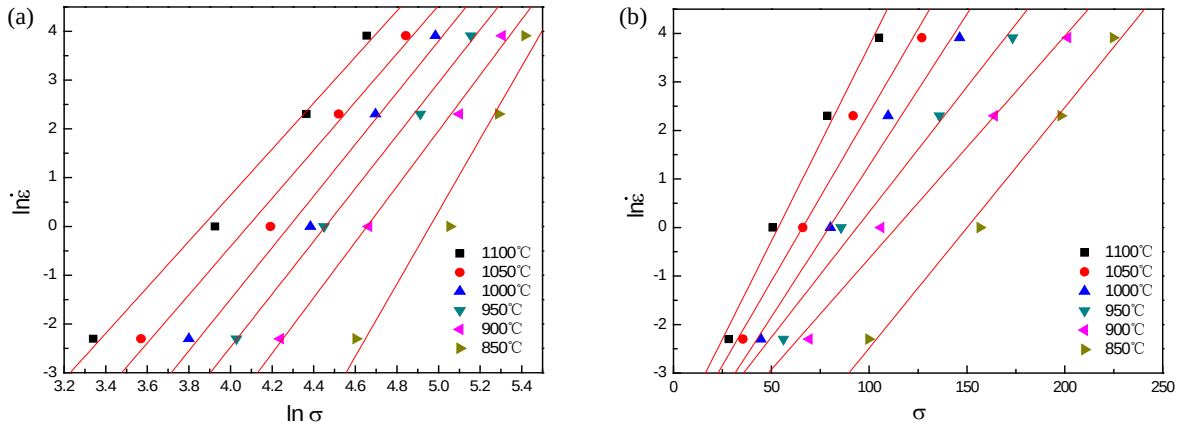

Fig. 4 Dependence of $\ln \dot{\varepsilon}$ on (a) $\ln \sigma$, and (b) σ of the 430lr FSS.

The activation energy of hot deformation is a significant parameter for representation the energy barrier to be overcome in metal processing. For a constant strain rate, by taking a partial differential of Eq. (8), the activation energy Q can be expressed as follows:

$$Q = Rn \cdot \left. \frac{\partial \ln[\sinh(\alpha\sigma)]}{\partial(1/T)} \right|_{\dot{\varepsilon}} \quad \text{(hyperbolic function)} \tag{9}$$

With the results of n and α, the value of Q can be obtained from the slopes of ln[sinh($\alpha\sigma$)] against 1000/T plots, as shown in Fig. 5(b).

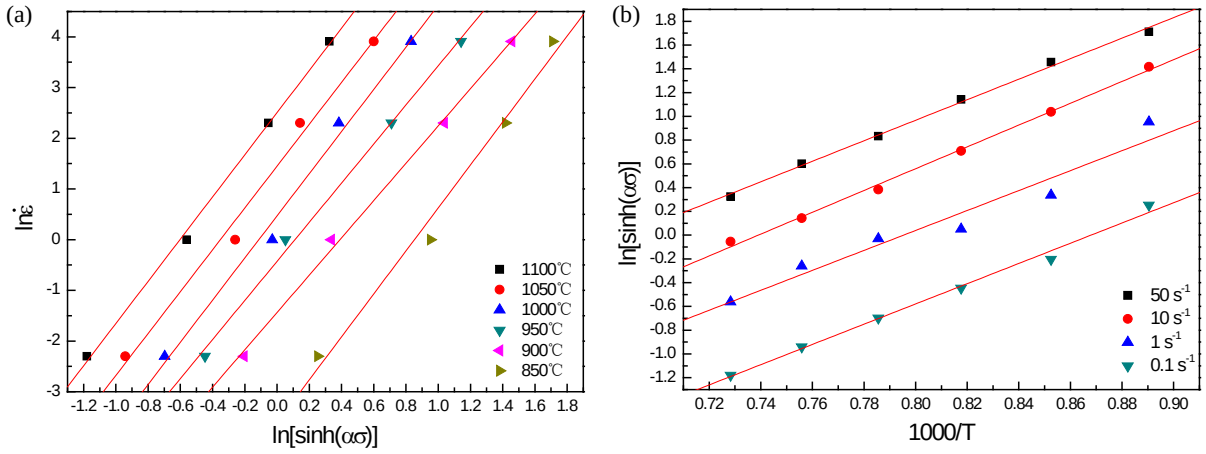

Fig. 5 Dependence of (a) ln $\dot{\varepsilon}$ on ln[sinh($\alpha\sigma$)], and (b) ln[sinh($\alpha\sigma$)] on 1000/T of the 430lr FSS.

The effect of strain on the flow stress behaviour is not considered in the Arrhenius-type constitutive model. The strain, however, affects significantly on the flow stress behaviour, especially under low temperature and high strain rate. In this study, the values of n_1, n_2, n, α, $Q_{hyperbolic}$ and ln$A$ in the strain range of 0.1~0.9 with an incremental strain of 0.1 were calculated, and the results are listed in Table 1. The relationship between the α, n, $Q_{hyperbolic}$, ln$A$, and the strain were established, as shown in Fig. 6. It is obviously illustrated that the strain has a significant effect on the material constants in the entire strain range by fourth order polynomial fitting, the material constants can be represented as Eq. (10) at a given strain.

Table.1 the calculated values of n_1, n_2, n, α, $Q_{hyperbolic}$ and ln$A$ at strains of 0.1~0.9

	n_2	n_1	α	n	Q hyperbolic	lnA
0.1	0.079268	6.630598	0.011955	4.812132	329.2711	31.59304446
0.2	0.064602	5.982313	0.010799	4.321998	306.7859	29.42470493
0.3	0.060388	5.699897	0.010595	4.119443	296.234	28.32442636
0.4	0.059472	5.579837	0.010658	4.032245	288.96857	27.94488221
0.5	0.059925	5.586367	0.010727	4.036695	291.37233	27.99461438
0.6	0.061338	5.593565	0.010966	4.03934	294.4075	28.23803325
0.7	0.06221	5.625758	0.011058	4.056932	298.2865	28.49541768
0.8	0.062947	5.622147	0.011196	4.056947	297.1077	28.64291501
0.9	0.063455	5.60235	0.011326	4.039935	299.24531	28.61254102

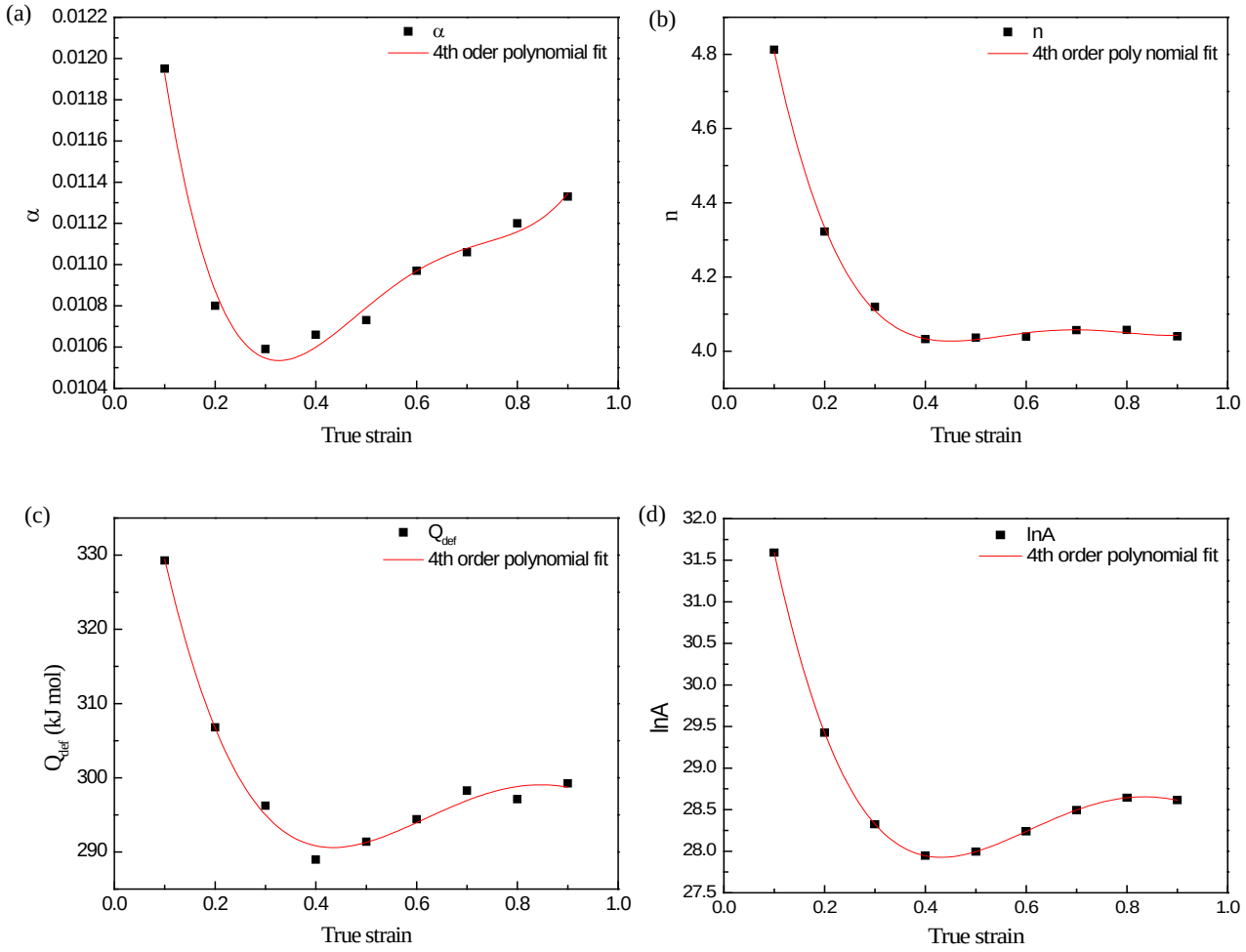

Fig. 6 Relationship between the (a) α, (b) n, (c) $Q_{hyperbolic}$, (d) ln$A$ and the true strain of the 430LR FSS.

$$\begin{cases} \alpha = 0.01414 - 0.02958\varepsilon + 0.08403\varepsilon^2 - 0.09629\varepsilon^3 + 0.03957\varepsilon^4 \\ n = 5.65537 - 10.80082\varepsilon + 25.84871\varepsilon^2 - 26.34543\varepsilon^3 + 9.71871\varepsilon^4 \\ Q_{\text{def}} = 367.09669 - 465.69186\varepsilon + 967.51747\varepsilon^2 - 784.87143\varepsilon^3 + 212.1972\varepsilon^4 \\ \ln A = 35.23264 - 45.23589\varepsilon + 96.28319\varepsilon^2 - 81.16629\varepsilon^3 + 23.27853\varepsilon^4 \end{cases} \tag{10}$$

Based on Eqs. (3) and (4), the relationship between the flow stress and Z parameter can be built like the following formula:

$$\sigma = \frac{1}{\alpha}\ln\left\{\left(\frac{Z}{A}\right)^{1/n} + \left[\left(\frac{Z}{A}\right)^{2/n} + 1\right]^{1/2}\right\} \tag{11}$$

Under a special strain, the Z parameters at different temperatures and strain rates can be easily calculated by Eq. (5). At the strain of 0.9, the relationship between lnZ and stress is shown in Fig.

7. By linear fitting, the slop and intercept can be acquired. Obviously, the Z parameter and the stress present typically positive correlation.

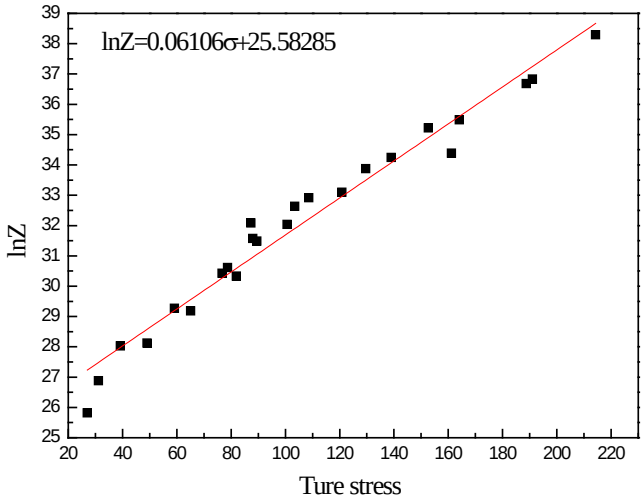

Fig. 7 The relationship between the lnZ and the true stress of the 430LR FSS at the stain of 0.9.

Fig. 8 shows the Z parameter map in the various temperature and strain rate at the strain of 0.9. From the map, it can be clearly obtained that the Z parameter increased with reducing temperature and rising strain rate. To some extent, the value of Z parameter reflects the microstructural characteristic during hot deformation. A lower Z parameter is beneficial to flow softening and DRX, whereas a higher Z parameter favours DRV occurring [39]. Therefore, the Z parameter level also has a good correlation with the grain size due to the restoration mechanism [40, 41].

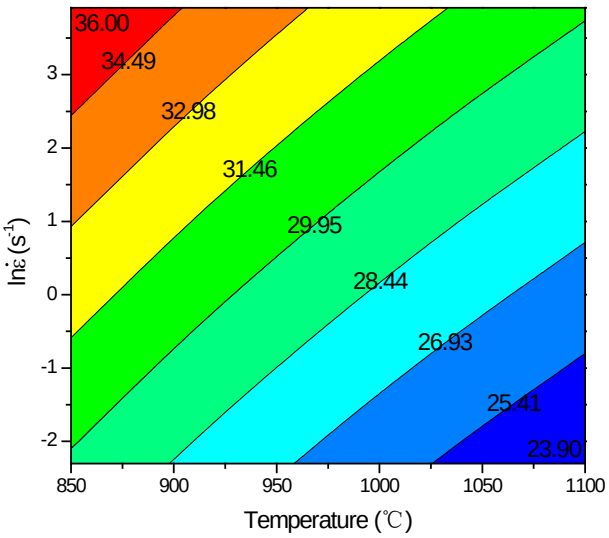

Fig. 8 Zener-Hollomon parameter map of the 430LR FSS at the strain of 0.9.

The comparison between the predicted flow stress values and the measured flow stress curves are presented in Fig. 9. The predicted flow stress exhibits a good agreement with the measured flow stress at higher strain rates or higher temperatures. However, at lower strain rates and lower

temperature, the prediction cannot keep highly confident with the real flow behaviour of the 430LR FSS.

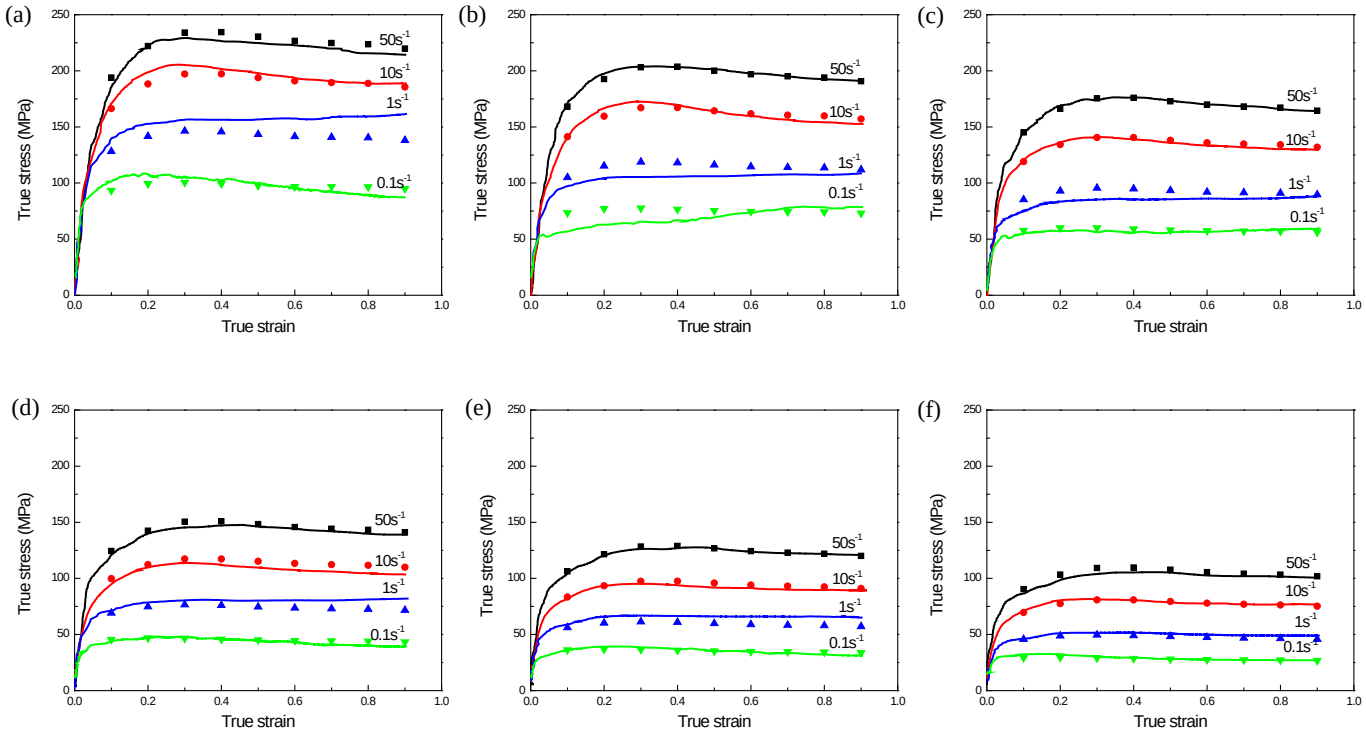

Fig. 9 Comparison between the measured and predicted flow stress at strain rates of 0.1～50 s^{-1} at (a) 850 ℃, (b) 900 ℃, (c) 950 ℃, (d) 1000 ℃, (e) 1050 ℃, and (f) 1100 ℃

In order to further quantitatively evaluate the Arrhenius-type constitutive equation, the standard statistical parameter of correlation coefficient R was used as follows:

$$R = \frac{\sum_{i=1}^{N}(M_i - \overline{M})(P_i - \overline{P})}{\sqrt{\sum_{i=1}^{N}(M_i - \overline{M})^2 \sum_{i=1}^{N}(P_i - \overline{P})^2}} \tag{12}$$

where M_i is the measured flow stress value and P_i is the predicted flow stress value. $\overline{M}$ and $\overline{P}$ are the mean values of M_i and P_i, respectively. N is the number of data points. The correlation coefficient R is a statistical measure to evaluate the reliability of the constitutive equation. Fig. 10 shows the correlation between the predicted and measured flow stress. It can be seen that most of the data point is close to the 45-line.

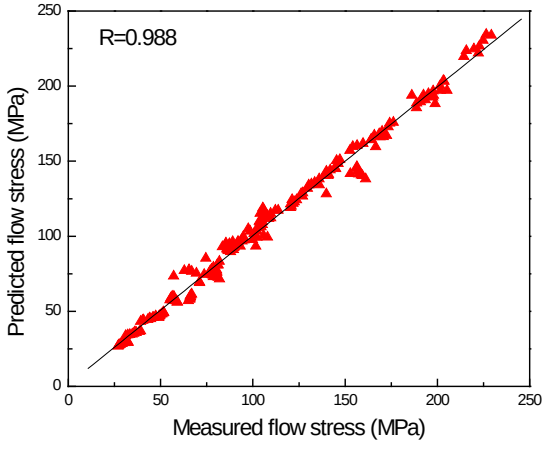

Fig. 10 Comparison between the measured and predicted flow stress values.

3.3 Microstructure evolution

The detailed study of microstructure evolution by large stain deformation with wild range temperatures and strain rates is significant for understanding actual industrial thermal mechanical processing and thereby exploring routing to restrict ridging [15, 16]. Compared with cylindrical compression, the plane strain compression, besides distinguishing deformation direction (RD, TD, ND), can realize the observation of elevated temperature deformed and undeformed microstructure in one specimen. The undeformed microstructures of specimens at the strain rate of 0.1 s^{-1} at 850 °C as well as 1100 °C are presented in Fig. 11. It is clearly seen that the two undeformed microstructures are composed of complete ferritic equiaxed grains with the average grain sizes no obvious difference. It means the microstructure of each specimen before deformation is similar, although the final holding temperature is different.

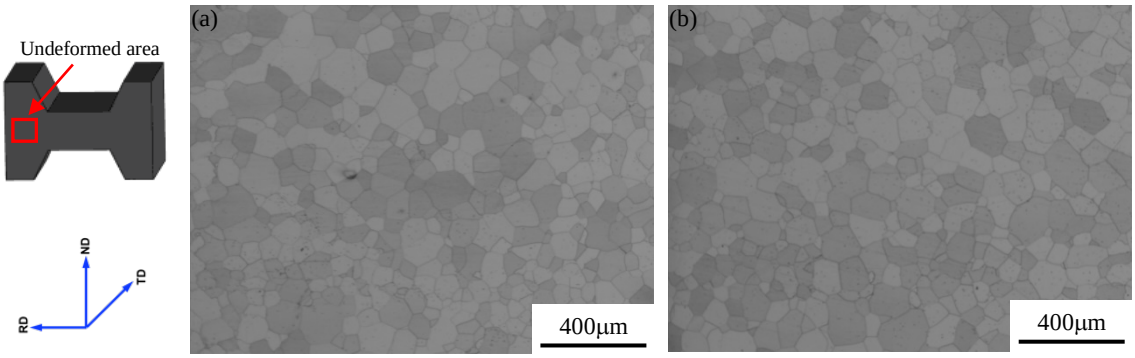

Fig. 11 Microstructures of the undeformed area of specimens at a strain rate of 0.1 s^{-1} and deformation temperature of (a) 850 °C, and (b) 1100 °C.

The evolution of microstructures of 430LR FSS after plane strain compression at various temperatures with the strain rate of 0.1 s^{-1} to the true strain of 0.9 is shown in Fig. 12. The deformed microstructures mainly consist of elongated grains and new recrystallized grains, obviously different with the undeformed microstructures (Fig. 11). In the case of deformed at 850 °C (Fig. 12(a)), the initial grains exhibit elongated in the direction of RD, like normal cold-rolled microstructure, and the deformation is inhomogeneous. A part of deformed grains contain an amount of substructure (as marked green arrows), and some other deformed grains with less substructure (as marked red arrows). In response to the strain asymmetrical distribution, the initial high angle grain boundaries, under thermal activation, migrate from the mild strain side to the severe strain side (as an insert in Fig. 12(a) and marked by blue arrows). The serrated boundaries, especially local bulges, imply the initial stage of DRX by the strain-induced grain boundary migration. At 900 °C (Fig. 12(b)), the substructure is more obvious, and the grain boundaries bulge into neighbouring grains more seriously (as marked blue arrows). Furthermore, newly fine recrystallized grains spread along the serrated boundaries (as an insert in Fig. 12(b) and marked by blue arrow). Increasing the

deformation temperature up to 950 °C (Fig. 12(c)), the deformation structure is characterized by elongated initial grain with more fine grains along the original grain boundaries (as marked green arrows). Due to the increase in deformation temperature, dislocation climb and cross-slip occur more readily, which lead to the formation of low angle boundaries, even substructures observed within severe deformed initial grains (as marked red rectangle).

The fraction and size of recrystallized grains increases with further increasing the temperature from 1000 °C to 1100 °C (as Fig. 12(d), (e), (f)), due to the grain boundary migration are accelerated by increasing temperature. The average new recrystallized grain sizes are around 4 mm, 18 mm, and 21 mm, respectively. Some of the new grains are elongated slightly marked with blue arrows, indicating the occurrence of grain growth simultaneous with grain deformation. It can be detected the amount of recrystallized grains spread along the original boundaries. Some substructure like boundary segments develops within a part of deformed grains, which reveals that the dislocation motion and reaction occur preferentially at the local high strain area (as marked green circles). Moreover, some deformed grains seems clear within less substructure formed (as marked red arrows), which relate with the grain orientation [12]. The microstructure of which deformed at 1000 °C is the most promiscuous.

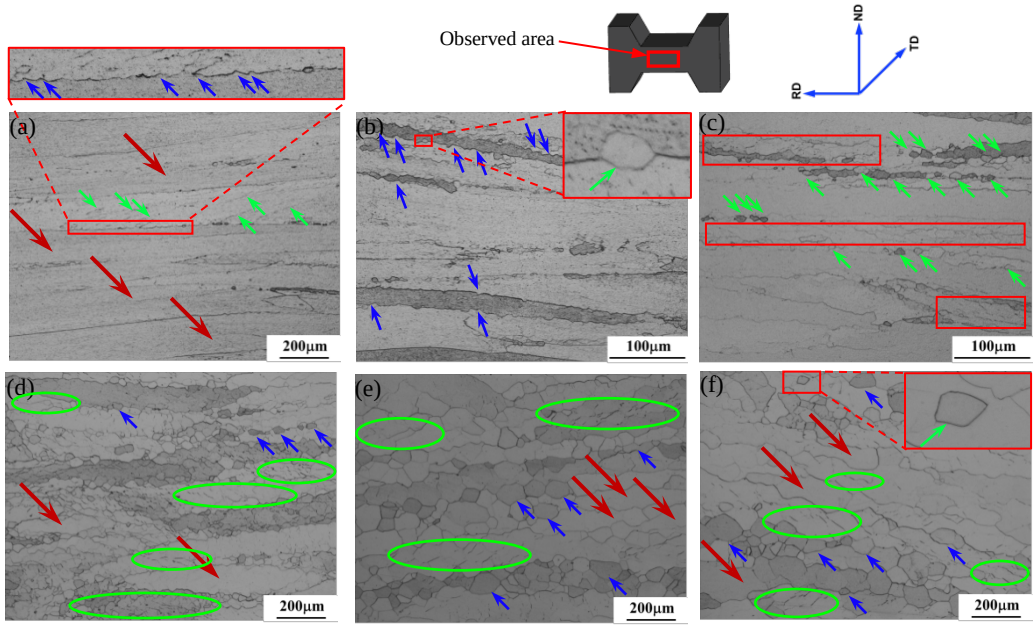

Fig. 12 Microstructures of 430lr deformed at the strain rate of 0.1 s^{-1} and temperature of (a) 850 ℃, (b) 900 ℃, (c) 950 ℃, (d) 1000 ℃, (e) 1050 ℃, and (f) 1100 ℃.

Substructures at the deformed centre part are presented by TEM of the specimen at 850 °C with a strain rate of 0.1s^{-1} shown in Fig. 13. Fig. 13(a) reveals that a large amount of (sub)grains were formed in the deformed matrix, which seems markedly different with the microstructure shown in Fig. 12(a). The (sub)grain sizes are around 2-4 μm, and all the (sub)grains elongate along the RD direction. Moreover, the amount of dislocation substructures in (sub)grain interior illustrate that the newly formed (sub)grains underwent plastic deformation during nucleation and growth process, as shown in the magnification image (Fig. 13(b)). The majority of dislocation spread individual and

some dislocation pile-up in the (sub)grain. In addition, some dislocations intersect each other by multiple slips.

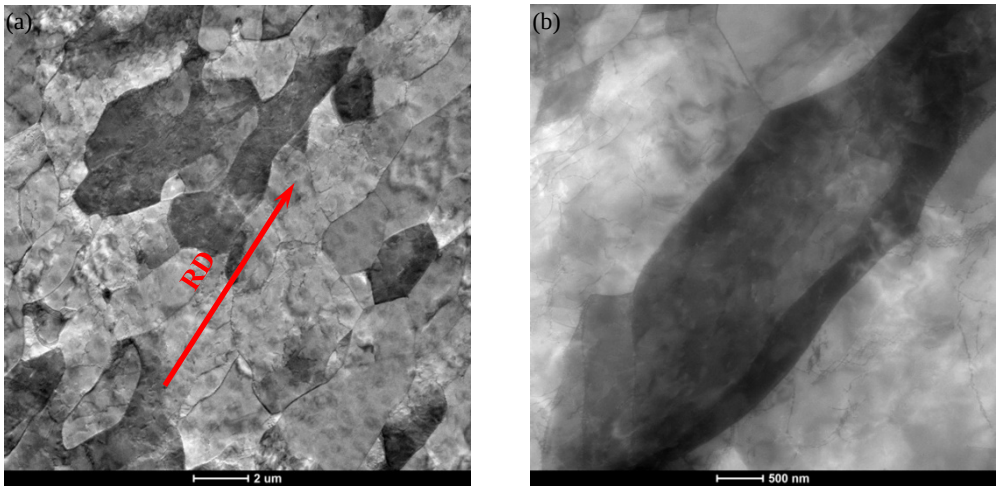

Fig. 13 Bright-field TEM micrographs of the specimen deformed at 850 °C with a strain rate of 0.1s^{-1}, (a) and (b) showing different magnifications.

The variations of microstructure at different deformed temperatures with a strain rate of 50s^{-1} are shown in Fig. 14. It is easy to be detected that the DRX is facilitated by the increase of temperature, as similar tendency with Fig. 12. It should, however, be noticed that, compared with the one deformed at the strain rate of 0.1s^{-1} (Fig. 12), the DRX is more obvious for the specimens deformed at the strain rate of 50 s^{-1}. Such as, some new grains along the original boundaries or within deformed grain were detected in the latter (Fig. 14(b), marked green arrows and red rectangle), only original boundaries migrated was prominent in the former at 900 °C (Fig. 12(b)). The new grain boundaries seem straighter at the strain rate of 50s^{-1}. These phenomena indicate that the higher strain rate accelerates the DRX. Normally, it is accepted that the grain growth would be enhanced at the lower strain rate, because of the longer time available for grain boundary migration [24, 42]. Some researchers also proposed that the higher strain rate can accelerate the DRX process in austenite, due to the adiabatic heat generated by elevated strain rate [42-44].

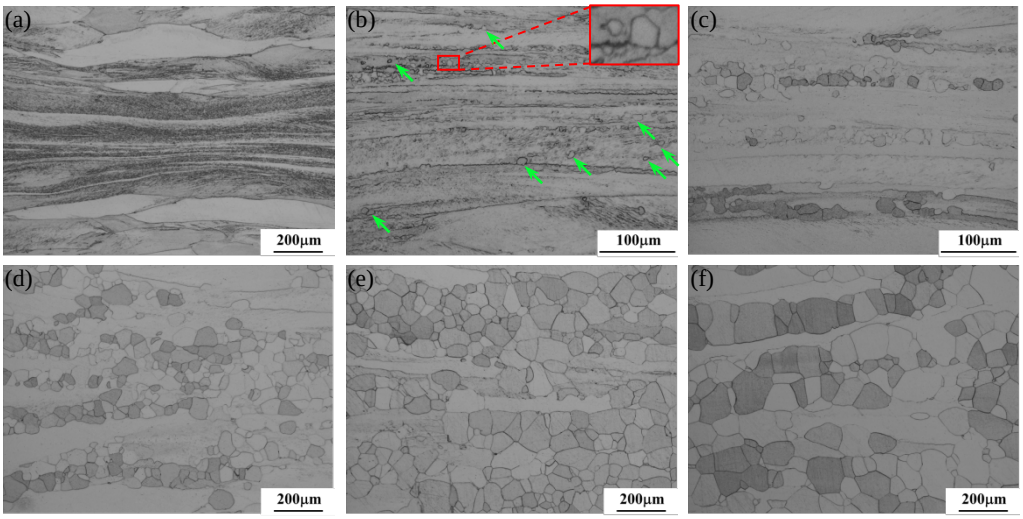

Fig. 14 Microstructures of 430LR deformed at the strain rate of 50 s^{-1} and temperature of (a) 850 ℃,

(b) 900 ℃, (c) 950 ℃, (d) 1000 ℃, (e) 1050 ℃, and (f) 1100 ℃.

In order to determine the influence of strain rate on the DRX, the microstructure of specimens after deformed at 1100 ℃ with different stain rates are presented in Fig. 15. It can clearly be seen that the DRX rate has no simple linear relationship with the increase of strain rate. When the strain rate is lower than 1 s^{-1}, the DRX fraction and grain size show an inverse tendency with the increase of strain rate. In contrast, the DRX is facilitated by elevated strain rate higher than 1 s^{-1}. The flow stress curves of strain rate at 10 s^{-1} and 50 s^{-1} exhibit an obvious softening stage after peak stress, as shown in Fig. 3, which highly relates with the microstructure evolution. This is, except for the adiabatic heat, the DRX behaviour is another significant factor for flow softening in the present study at strain rate of 10 s^{-1} and 50 s^{-1}.

Generally, the DRX fraction and grains size of high stacking fault energy metals tend a negative correlation with strain rate [33], which is opposite with the results of the present study. It has, however, been reported that the DRX mechanisms transfer between continuous and discontinuous DRX in high stacking fault energy metals, depending on the deformed conditions, which lead to different DRX rates [15]. In the case of low strain rate, the continuous DRX plays a prominent role in microstructure evolution, whereas at high strain rate, discontinuous DRX occurs rapidly. Similar microstructure characteristics were detected in a nickel-base superalloy with approximate stain rate parameters, despite it has markedly different stacking fault energy with current study [25]. The DRX behaviour has been a subject for metallurgists, but until now there is no unified view. It is well known that the microstructure is controlled by the competition of plastic deformation and DRX for hot compression. Moreover, the DRX is the combined contribution of stored energy, time duration, and deformation temperature. Due to the high stacking fault energy of ferrite, the dislocation slip and move easily. At the strain rate of 0.1 s^{-1}, vast of dislocations rearrangement and annihilation decreasing the nucleation rate. The new nuclei, however, have sufficient time to grow up, which lead to coarse grain size. When the strain rate increases to 1 s^{-1}, the reduction of DRX behaviour is mainly attributed to the short deformation time inhibiting the grain growth, while the stored energy is higher than the former. It can be concluded that the DRX behaviour is dominated by the growth process at low strain rates. Compared Fig. 14(a) with Fig. 13(a), it is clearly illustrated that the specimen deformed at high strain rate is much significant than the one at low strain rate. At high strain rate, no enough time for dislocation rearrangement, high-density dislocations are generated and piled up within the deformed matrix. More deformed energy is rapidly stored with elevating strain rate. Once the stored energy is higher than a critical condition, under thermal activated conditions, the DRX nucleation and growth rate will be dramatically enhanced [25]. Even the duration time of deformation reduced exponentially at high strain rate, the DRX fraction and grain size are accelerated as the strain rate above 1s^{-1}.

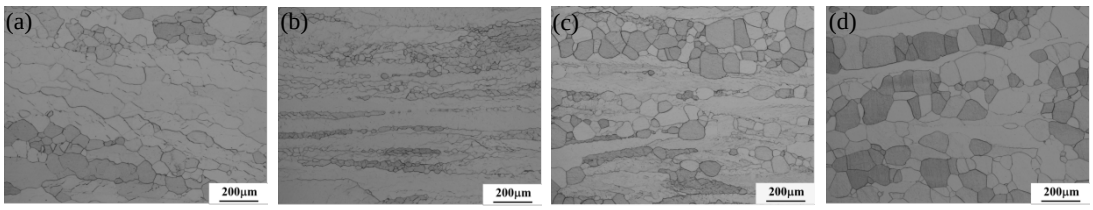

Fig. 15 Microstructures of 430LR deformed at 1100 ℃ with different strain rates: (a) 0.1 s^{-1}, (b) 1 s^{-1}, (c) 10 s^{-1}, and (d) 50 s^{-1}.

4. Conclusions

The effect of temperature and strain rate on hot deformation behaviour of a 430LR FSS has been studied. Plane strain compression tests were carried out by a Gleeble 3500 thermal-mechanical test simulator with a hydrawedge system under a high strain (true strain of 0.9) and wide ranges of deformation temperatures (850-1100 °C) and strain rates (0.1-50 s^{-1}). The main conclusions can be summarized as follows:

(1) The flow stress increased with the increase of the strain rate and decrease of the temperature. Under high strain rate, the flow stress curves exhibited a drop in the flow stress after a peak value.

(2) The modified constitutive equation which used to predict flow stress has a good agreement with the measured flow stress, except 850 °C in 1 s^{-1}. The Z parameter decreases with the decrease of the strain rate and increase of the temperature.

(3) With increasing the deformation temperature, the dynamic recrystallization grain size and fraction increase. Due to the inhomogeneous deformation, the local original grain boundaries migrate toward high strain side, lead to new grains formation.

(4) Under low strain rate, with the increase of the strain rate, the DRX is inhibited by shortening duration time. However, under high strain rate, both the adiabatic heating and high stored energy accelerate the DRX. Due to the multifactor functioning, the DRX shows a non-linear relationship with strain rate.

Acknowledgement

The authors acknowledge the financial supports from the Baosteel-Australia Joint Research and Development Centre project (B14014), the National Natural Science Foundation of China (No. 51701021) and Science and Technology Research Project of Education Department of Jilin Province of China (No. JJKH20181028KJ).

References

[1] S. Patra, A. Ghosh, J. Sood, L. Singhal, A. Podder, D. Chakrabarti, Effect of coarse grain band on the ridging severity of 409L ferritic stainless steel, Materials & Design 106 (2016) 336-348.
[2] H.-J. Shin, J.-K. An, S.H. Park, D.N. Lee, The effect of texture on ridging of ferritic stainless steel, Acta Materialia 51(16) (2003) 4693-4706.
[3] S. Mehtonen, L. Karjalainen, D. Porter, Hot deformation behavior and microstructure evolution of a stabilized high-Cr ferritic stainless steel, Materials Science and Engineering: A 571 (2013) 1-12.
[4] S. Mehtonen, E. Palmiere, D. Misra, P. Karjalainen, D. Porter, Microstructural and texture development during multi-pass hot deformation of a stabilized high-chromium ferritic stainless steel, ISIJ international 54(6) (2014) 1406-1415.

[5] R. Siqueira, H. Sandim, T. Oliveira, D. Raabe, Composition and orientation effects on the final recrystallization texture of coarse-grained Nb-containing AISI 430 ferritic stainless steels, Materials Science and Engineering: A 528(9) (2011) 3513-3519.
[6] K.H. Lo, C.H. Shek, J. Lai, Recent developments in stainless steels, Materials Science and Engineering: R: Reports 65(4-6) (2009) 39-104.
[7] J. Mola, I. Jung, J. Park, D. Chae, B.C. De Cooman, Ridging control in transformable ferritic stainless steels, Metallurgical and Materials Transactions A 43(1) (2012) 228-244.
[8] C.-z. Lu, Z. Fang, J.-y. Li, Influence of differential speed rolling ratio on the ridging behavior of ultra purified 17% Cr ferritic stainless steel, Materials Characterization 135 (2018) 257-264.
[9] F. Gao, Z. Liu, R. Misra, H. Liu, F. Yu, Constitutive modeling and dynamic softening mechanism during hot deformation of an ultra-pure 17% Cr ferritic stainless steel stabilized with Nb, Metals and Materials International 20(5) (2014) 939-951.
[10] X. Zhang, L. Fan, Y. Xu, J. Li, X. Xiao, L. Jiang, Effect of aluminum on microstructure, mechanical properties and pitting corrosion resistance of ultra-pure 429 ferritic stainless steels, Materials & Design 65 (2015) 682-689.
[11] Y. Shan, X. Luo, X. Hu, S. Liu, Mechanisms of solidification structure improvement of ultra pure 17 wt% Cr ferritic stainless steel by Ti, Nb addition, Journal of Materials Science & Technology 27(4) (2011) 352-358.
[12] F.J. Humphreys, M. Hatherly, Recrystallization and related annealing phenomena, Elsevier2012.
[13] S.-I. Kim, Y.-C. Yoo, Continuous dynamic recrystallization of AISI 430 ferritic stainless steel, Metals and Materials International 8(1) (2002) 7.
[14] F. Gao, B. Song, Y. Xu, K. Xia, Substructural changes during hot deformation of an Fe-26Cr ferritic stainless steel, Metallurgical and Materials Transactions A 31(1) (2000) 21-27.
[15] C. Castan, F. Montheillet, A. Perlade, Dynamic recrystallization mechanisms of an Fe–8% Al low density steel under hot rolling conditions, Scripta Materialia 68(6) (2013) 360-364.
[16] J.-H. Kang, S. Torizuka, Dynamic recrystallization by large strain deformation with a high strain rate in an ultralow carbon steel, Scripta Materialia 57(11) (2007) 1048-1051.
[17] S. Chen, R. Rana, A. Haldar, R.K. Ray, Current state of Fe-Mn-Al-C low density steels, Progress in Materials Science 89 (2017) 345-391.
[18] S. Mehtonen, E. Palmiere, R. Misra, L. Karjalainen, D. Porter, Dynamic restoration mechanisms in a Ti–Nb stabilized ferritic stainless steel during hot deformation, Materials Science and Engineering: A 601 (2014) 7-19.
[19] N. Haghdadi, P. Cizek, H. Beladi, P. Hodgson, A novel high-strain-rate ferrite dynamic softening mechanism facilitated by the interphase in the austenite/ferrite microstructure, Acta Materialia 126 (2017) 44-57.
[20] P. Cizek, The microstructure evolution and softening processes during high-temperature deformation of a 21Cr–10Ni–3Mo duplex stainless steel, Acta Materialia 106 (2016) 129-143.
[21] N. Haghdadi, A. Zarei-Hanzaki, E. Farabi, P. Cizek, H. Beladi, P. Hodgson, Strain rate dependence of ferrite dynamic restoration mechanism in a duplex low-density steel, Materials & Design 132 (2017) 360-366.
[22] Q. Yang, Z. Deng, Z. Zhang, Q. Liu, Z. Jia, G. Huang, Effects of strain rate on flow stress behavior and dynamic recrystallization mechanism of Al-Zn-Mg-Cu aluminum alloy during hot deformation, Materials Science and Engineering: A 662 (2016) 204-213.
[23] N. Park, A. Shibata, D. Terada, N. Tsuji, Flow stress analysis for determining the critical condition

of dynamic ferrite transformation in 6Ni–0.1 C steel, Acta Materialia 61(1) (2013) 163-173.
[24] Y. Liu, Z. Yao, Y. Ning, Y. Nan, Effect of deformation temperature and strain rate on dynamic recrystallized grain size of a powder metallurgical nickel-based superalloy, Journal of Alloys and Compounds 691 (2017) 554-563.
[25] H. Jiang, J. Dong, M. Zhang, Z. Yao, A study on the effect of strain rate on the dynamic recrystallization mechanism of alloy 617B, Metallurgical and Materials Transactions A 47(10) (2016) 5071-5087.
[26] D. Raabe, Z. Zhao, S.-J. Park, F. Roters, Theory of orientation gradients in plastically strained crystals, Acta Materialia 50(2) (2002) 421-440.
[27] T. Sakai, J.J. Jonas, Overview no. 35 dynamic recrystallization: mechanical and microstructural considerations, Acta Metallurgica 32(2) (1984) 189-209.
[28] R. Doherty, D. Hughes, F. Humphreys, J. Jonas, D.J. Jensen, M. Kassner, W. King, T. McNelley, H. McQueen, A. Rollett, Current issues in recrystallization: a review, Materials Science and Engineering: A 238(2) (1997) 219-274.
[29] H.J. McQueen, N. Ryan, Constitutive analysis in hot working, Materials Science and Engineering: A 322(1-2) (2002) 43-63.
[30] H. Mirzadeh, Constitutive modeling and prediction of hot deformation flow stress under dynamic recrystallization conditions, Mechanics of Materials 85 (2015) 66-79.
[31] J. Zhao, Z. Jiang, G. Zu, W. Du, X. Zhang, L. Jiang, Flow behaviour and constitutive modelling of a ferritic stainless steel at elevated temperatures, Metals and Materials International 22(3) (2016) 474-487.
[32] S. Mehtonen, L. Karjalainen, D. Porter, Modeling of the high temperature flow behavior of stabilized 12–27 wt% Cr ferritic stainless steels, Materials Science and Engineering: A 607 (2014) 44-52.
[33] N. Nayan, N.P. Gurao, S.N. Murty, A.K. Jha, B. Pant, S. Sharma, K.M. George, Microstructure and micro-texture evolution during large strain deformation of an aluminium–copper–lithium alloy AA 2195, Materials & Design 65 (2015) 862-868.
[34] Y. Han, G. Qiao, J. Sun, D. Zou, A comparative study on constitutive relationship of as-cast 904L austenitic stainless steel during hot deformation based on Arrhenius-type and artificial neural network models, Computational Materials Science 67 (2013) 93-103.
[35] J. Liu, H. Chang, R. Wu, T. Hsu, X. Ruan, Investigation on hot deformation behavior of AISI T1 high-speed steel, Materials characterization 45(3) (2000) 175-186.
[36] Y. Lin, X.-M. Chen, A critical review of experimental results and constitutive descriptions for metals and alloys in hot working, Materials & Design 32(4) (2011) 1733-1759.
[37] C.M. Sellars, W. McTegart, On the mechanism of hot deformation, Acta Metallurgica 14(9) (1966) 1136-1138.
[38] C. Zener, J.H. Hollomon, Effect of strain rate upon plastic flow of steel, Journal of Applied physics 15(1) (1944) 22-32.
[39] D. Zou, Y. Han, D. Yan, D. Wang, W. Zhang, G. Fan, Hot workability of 00Cr13Ni5Mo2 supermartensitic stainless steel, Materials & Design 32(8-9) (2011) 4443-4448.
[40] A. Ammouri, G. Kridli, G. Ayoub, R. Hamade, Relating grain size to the Zener–Hollomon parameter for twin-roll-cast AZ31B alloy refined by friction stir processing, Journal of Materials Processing Technology 222 (2015) 301-306.
[41] Y. Li, Y. Zhang, N. Tao, K. Lu, Effect of the Zener–Hollomon parameter on the microstructures and mechanical properties of Cu subjected to plastic deformation, Acta Materialia 57(3) (2009) 761-772.

[42] H. Zhang, K. Zhang, H. Zhou, Z. Lu, C. Zhao, X. Yang, Effect of strain rate on microstructure evolution of a nickel-based superalloy during hot deformation, Materials & Design 80 (2015) 51-62.
[43] J.T. Benzing, W.A. Poling, D.T. Pierce, J. Bentley, K.O. Findley, D. Raabe, J.E. Wittig, Effects of strain rate on mechanical properties and deformation behavior of an austenitic Fe-25Mn-3Al-3Si TWIP-TRIP steel, Materials Science and Engineering: A 711 (2018) 78-92.
[44] Y. Cao, H. Di, J. Zhang, J. Zhang, T. Ma, R. Misra, An electron backscattered diffraction study on the dynamic recrystallization behavior of a nickel–chromium alloy (800H) during hot deformation, Materials Science and Engineering: A 585 (2013) 71-85.